International Journal of Nanomedicine

Dovepress
Taylor & Francis Group

Open Access Full Text Article

ORIGINAL RESEARCH

Folate-Functionalized CS/rGO/NiO Nanocomposites as a Multifunctional Drug Carrier with Anti-Microbial, Target-Specific, and Stimuli-Responsive Capacities

Sreekanth Reddy Obireddy[1,*], Arumugam Ayyakannu[2,*], Gopinath Kasi[3], Badrinathan Sridharan[4], Wing-Fu Lai[5], Karthika Viswanathan[6,7]

[1]Department of Urology, Zhejiang Provincial People's Hospital, Affiliated People's Hospital, Hangzhou Medical College, Zhejiang, 310014, People's Republic of China; [2]Department of Botany, Alagappa University, Karaikudi, Tamil Nadu, 630 003, India; [3]School of Materials and Energy, Southwest University, Chongqing, 400715, People's Republic of China; [4]Department of Biomedical Engineering, Pukyong National University, Busan, 48513, Republic of Korea; [5]School of Food Science and Nutrition, University of Leeds, Leeds, LS2 9JT, UK; [6]Department Nanoscience and Technology, Alagappa University, Karaikudi, Tamil Nadu, 630 003, India; [7]Department of Health Sciences, The Graduate School of Dong-A University, Busan, 49315, Republic of Korea

*These authors contributed equally to this work

Correspondence: Wing-Fu Lai; Karthika Viswanathan, Email rori0610@graduate.hku.hk; karthikanano2021@gmail.com

Purpose: This study reports the synthesis of surface-modified chitosan (CS) coated with reduced graphene oxide/nickel oxide (rGO/NiO) as a multifunctional drug carrier with anti-microbial, target-specific, and stimuli-responsive capacities. CS, rGO, and NiO nanoparticles are selected due to their pH-responsiveness, large surface area, and ROS generating-capacity, respectively.

Methods: The CS/rGO/NiO nanocomposites (NCs) are synthesized using a solvothermal approach. Glutaraldehyde is used to crosslink CS and rGO/NiO to enhance the stability of the NCs. Structural properties, magnetic properties, antimicrobial activity, drug release sustainability and toxicity of the NCs are evaluated.

Results: The NCs show good biocompatibility, excellent magnetic properties, good target specificity, and remarkable cell growth inhibitory effects. The release of doxorubicin (DOX) from the drug-loaded NCs at pH 5.0 (~98.6%) is much higher than that at pH 7.4 (~9.6%). Furthermore, the NCs inhibit the growth of A549 and MCF7 cells, causing the viability of A549 and MCF7 to drop to 12.3% and 7.1%, respectively. By using zebrafish embryos as a model, no detectable change is observed in the survival rate of the embryos after NC treatment.

Conclusion: The NCs exhibit multifunctional, target-specific, and pH-responsive characteristics. These properties make the NCs a promising candidate for use in drug delivery applications.

Keywords: nickel oxide, nanoparticles, biopolymer, folate receptor, drug delivery

Introduction

Recent advances in nanotechnology have enabled the design of multifunctional drug delivery systems. Over the last several decades, metal oxide nanoparticles (NPs) have drawn considerable attention because of their small size, large surface area, ability to absorb light, and enhanced chemical reactivity.[1] These characteristics render them appropriate for diverse biomedical applications, ranging from drug delivery to cancer therapy.[2] Among various metal oxide NPs, nickel oxide (NiO) NPs have garnered special research interest. NiO NPs induce oxidative stress in cells by causing ion migration toward the nuclear cell membrane, and hence show therapeutic potential in a variety of tumors.[3–5] This has recently been verified by Kouhbanani et al,[6] who demonstrated the effect of NiO NPs in acting against the growth of Hep-G2, MCF-7 and HT-29 cancer cells.

Received: 11 October 2024
Accepted: 25 January 2025
Published: 14 February 2025

In addition to metal oxide NPs, reduced graphene oxide (rGO) show great potential for use in controlled drug delivery due to its significant water dispersibility, ease of surface functionalization, and excellent biocompatibility.[7,8] In addition, the presence of various functional groups (eg, hydroxyl groups, epoxy groups, carbonyl groups and π-conjugated systems) improves the drug encapsulation efficiency of rGO.[9] A combination of rGO and metal oxide NPs can exhibit synergistic anticancer properties. This has been evidenced by the fact that MnO_2/rGO nanocomposites (NCs) exhibit anticancer effects against A549 cells.[10] A similar observation has been made on curcumin-loaded CS-Fe_3O_4-rGO NCs[11] and DOX-loaded CS-Fe_3O_4-rGO NCs.[12] Both of them have been reported to show anticancer activity against MCF7 cells. In the current study, we apply both NiO NPs and rGO to generate NCs for use in drug delivery, with chitosan (CS) (which is a natural biopolymer containing hydroxyl and amine groups) being the polymeric component in the NC formulation.[9] We hypothesize that the presence of rGO can enhance the efficiency of drug encapsulation. Furthermore, folic acid (FA) has been extensively used in the literature as a targeting ligand.[13] It can covalently bind to chitosan through its γ-carboxyl moiety while maintaining a strong affinity towards folate receptors.[14] FA is, therefore, adopted in this study for functionalization of the generated NCs.

Furthermore, CS is biocompatible, non-toxic, pH-sensitive, and mucoadhesive.[12] Its mucoadhesive property, along with its ability to open tight junctions, enhances transmucosal absorption and antitumor effects of chemotherapeutic agents. Encapsulation of rGO into the polymeric matrix will preserve the activity of rGO while ameliorating its toxicity. The major advantage of using CS and NPs for drug delivery is that they can increase drug solubility, extend the blood circulation time of the delivered drug and reduce systemic toxicity.[15–18] In this study, we examine the drug delivery performance of the generated NCs by using doxorubicin (DOX) as a model drug. Upon being loaded with DOX, the pH-sensitive NCs exhibit good drug release sustainability and good affinity to the folate receptor through electrostatic absorption. Our results demonstrate the potential of the NCs to mediate target-specific drug delivery for future treatment development.

Materials and Methods

Chemicals

Nickel(II) chloride ($NiCl_2$), graphite powder, CS, $NaNO_3$, NaOH, $KMnO_4$, H_2SO_4, FA, glutaraldehyde, sucrose and ethylene glycol were purchased from Merck (India). Microbial culture media and strains were obtained from Himedia (India). Milli-Q water was used for all experiments. The microbial cultures [including *Bacillus subtilis* (ATCC 6633), *Staphylococcus aureus* (MTCC 1935) *Streptococcus pneumoniae* (MTCC 1936), *Escherichia coli* (MTCC 40), *Pseudomonas aeruginosa* (MTCC 2642), *Proteus vulgaris* (MTCC 7277), *Proteus mirabilis* (ATCC 7002), *Salmonella typhi* (MTCC 3224), *Shigella dysenteriae* (ATCC 23513), *Klebsiella pneumonia* (MTCC 432), fungi included *Aspergillus niger* (MTCC 16404), *Aspergillus fumigatus* (MTCC 9657) and *Candida albicans* (MTCC 3959)] were purchased from MTCC and ATCC.

Synthesis of Nickel Oxide NPs

NiO NPs were prepared by using a facile solvothermal method, in which $NiCl_2$ (0.1 M) and sucrose (0.1 mmol) were dissolved in ethylene glycol (50 mL) under vigorous stirring. The pH of the solution was adjusted to 12 by using NaOH. The reaction mixture was kept stirring for 30 min before it was transferred to a Teflon-lined stainless-steel autoclave reactor. The reactor was kept at 150°C for 24 h. It was then allowed to cool to room temperature. The supernatant was decanted. The product was isolated by using a permanent magnet. The obtained residue was washed four times using deionized water, freeze-dried and stored in airtight containers.

Synthesis of rGO/NiO NCs

Graphene oxide (GO) was prepared by using the modified Hummer's method as previously described.[12] Ten milligrams of GO was then dispersed in 10 mL of an aqueous solution of ethylene glycol. The suspension was subjected to ultrasonication for 3 h. Under constant stirring, sucrose and an aqueous solution (0.1 M) of $NiCl_2$ were added. The pH of the reaction mixture was adjusted to 12 by using NaOH. Ascorbic acid was added to reach the final

concentration of 0.001M. After one hour of stirring, the reaction mixture was transferred to a Teflon-lined autoclave reactor. The reactor was kept at 180 °C for 24 h. The product was collected, washed with water/acetone, separated by centrifugation, and freeze-dried.

Synthesis of CS/rGO/NiO NCs

CS was dissolved in a 2% (w/v) aqueous solution of acetic acid and was stirred for 48 h at room temperature. The pH of the reaction mixture was adjusted to 7. Ten milliliters of rGO/NiO NCs (0.3 mg/mL) was mixed with 5 mL of the CS solution [at different concentrations: 5% (w/v), 10% (w/v), 15% (w/v)] followed by 30 min of sonication. Glutaraldehyde (1%, 3 mL) was added to the reaction mixture. The mixture was stirred at 1000 rpm for 24 h. The product was washed by using Milli-Q water to obtain CS/rGO/NiO NCs.

Preparation of Folate-Conjugated CS/rGO/NiO NCs

Surface conjugation of CS/rGO/NiO (15%) NCs with folic acid was achieved by using the protocol previously described.[12] Briefly, 0.1 mg of folic acid and 0.05 μL of (3-aminopropyl)triethoxysilane (APTS) were dissolved in 1 mL of dimethyl sulfoxide (DMSO). About 0.03 mg of N-hydroxysuccinimide and 0.05 mg of 1-(3-dimethylamino-propyl)-3-ethylcarbodiimide hydrochloride were added. The reaction mixture was stirred for 2 hours at ambient conditions. After that, the solution was added to a flask in which 4 mL of toluene and 2mL of a DMSO suspension of CS/rGO/NiO NCs were mixed. The reaction mixture was stirred for 20 hours at room temperature. The folate-conjugated NCs were retrieved by centrifugation at 12,000 rpm for 30 minutes, washed multiple times with toluene, and dried under vacuum.

Structural Characterization

Fourier-transform infrared (FT-IR) spectroscopy was conducted using a Perkin-Elmer FT-IR spectrophotometer (Thermo Nicolet 380, USA) using the KBr pellet technique. The crystalline structures of the samples were analyzed using a PW3040/60 X'pert PRO X-ray diffractometer (PANalytical, EA Almelo, The Netherlands) equipped with Cu Kα radiation (λ = 1.54060 Å). The microstructure of the samples was examined using field-emission scanning electron microscopy (FE-SEM; Hitachi S-4500, USA), with the elemental composition determined by using energy-dispersive X-ray (EDX) spectroscopy. Morphological features and particle size of the samples were studied using high-resolution transmission electron microscopy (HR-TEM) performed on a Tecnai instrument. Samples for TEM analysis were prepared by drop-casting the suspension containing the sample onto carbon-coated copper grids, followed by removal of the excess solution using filter paper at ambient conditions. TEM analysis was conducted using a Tecnai F20 instrument operating at 200 kV. X-ray photoelectron spectroscopy (XPS; Carl Zeiss, Al Kα excitation at 250 W) was employed to analyze the chemical states of the samples. Magnetic measurements were conducted at room temperature using a vibrating sample magnetometer (VSM; Lake Shore, Model-7410, USA).

Analysis of Drug Loading and Release

A stock solution of DOX was prepared by dissolving 10 mg of DOX in 5 mL of PBS buffer (pH 7.4) for 10 minutes. The solution was diluted to other concentrations [0.05%(w/v), 1%(w/v), 1.5%(w/v), 2%(w/v), 2.5%(w/v), 3%(w/v), 3.5%(w/v), 4%(w/v), 4.5%(w/v) and 5%(w/v)] before use. CS/rGO/NiO/FA was added to each DOX solution to reach a final concentration of 100 μg/mL. The solution was then incubated for 24 hours. The DOX-loaded NCs were centrifuged at 12,000 rpm for 10 minutes. The pellet was stored at 4 °C before use. The concentration of DOX in the supernatant was determined by UV-visible spectroscopy at 481 nm. The amount of DOX loaded into NCs was quantified by comparing the concentration of DOX in the supernatant with the initial amount of DOX added. The rate of drug release from DOX-loaded CS/rGO/NiO/FA NCs was determined in PBS buffer at pH 7.4 and pH 5.5. Briefly, 5 mg of the DOX-loaded NCs was put inside a dialysis tubing, suspended in 10 mL of PBS (pH 7.4 and pH 5.5), and agitated constantly at 37°C. At regular time intervals, 2 mL of the release medium was withdrawn, and replaced with the same volume of fresh PBS. The concentration of DOX in the collected sample was determined by UV-visible spectroscopy at 481 nm. All the

measurements were done in triplicates. Release data were fitted to different kinetic models (zero-order, first-order, Higuchi, and Korsmeyer-Peppas models) to determine the kinetics of drug release as previously described.[19]

Determination of Antimicrobial Activity

Gram-positive (*Bacillus subtilis, Staphylococcus aureus*, and *Streptococcus pneumoniae*) and Gram-negative (*Escherichia coli, Proteus vulgaris, Proteus mirabilis, Pseudomonas aeruginosa, Salmonella typhi, Shigella dysenteriae*, and *Klebsiella pneumoniae*) bacteria were inoculated onto an agar plate, which was then incubated for 24 hours at 37°C. The fungi (*Aspergillus niger, Aspergillus fumigatus*, and *Candida albicans*) were allowed to grow on a potato dextrose agar plate using the well diffusion method and incubated at 37°C for 72 hours. To assess the antimicrobial activity of different samples (including GO, CS, NiO, rGO/NiO, and CS/rGO/NiO NCs), the samples were dissolved in DMSO. Discs containing one of the DMSO-dissolved samples were placed on an agar plate. DMSO (100 μL) was used as the negative control in this experiment. All agar plates were incubated at 37°C for 24 hours. The diameter of the inhibitory zone was determined in millimeters. All assays were conducted in triplicate.

Biocompatibility Studies

Wild-type AB strains of zebrafish (*Danio rerio*) embryos were purchased from a commercial ornamental fish farm, Madurai, Tamil Nadu, India. Stock solutions, at a concentration of 30 μg/mL, of different samples (including GO, CS, NiO, rGO/NiO, and CS/rGO/NiO) were prepared using double-distilled water. About 10 nL of the stock solution was injected into an embryo via microinjection. The embryos injected with NCs, as well as the control embryos (in which no NCs were administered), were incubated at 28 °C in the dark. Microscopic images were captured at regular time intervals (24, 36, 48 h). After 0 hours post fertilization (hpf) and 72 hpf, the abnormalities of the hatched fish were examined using a MicroFire camera (Olympus CX-21i Trinocular Microscope, LED illumination) mounted onto a Leica MZ16 stereo-microscope (Meyer Instruments, Houston, TX, USA).

Evaluation of Cytotoxicity

A549 and MCF7 cells were obtained from the National Centre for Cell Sciences (NCCS) in Pune, India. The cells were grown in Dulbecco's modified Eagles medium (DMEM) containing 2 mm l-glutamine and balanced salt solution (BSS) [comprising 1.5 g/L Na_2CO_3, 1 mm sodium pyruvate, 0.1 mm nonessential amino acids, 1.5 g/L glucose, 10 mm (4-(2-hydroxyethyl)-1-piperazineethane sulfonic acid) (HEPES)] (GIBCO, USA). The concentrations of penicillin and streptomycin (100 IU/100 g) in the cell culture medium were kept at 1 mL/L. The cells were kept at 37 °C and 5% CO_2. Changes in the viability of cells treated with pure NCs, pure DOX, and DOX-loaded NCs were examined as previously described.[12] Morphological changes of the treated cells were examined by using a previously reported protocol.[12]

Statistical Analysis

The data were statistically analyzed using one-way analysis of variance (ANOVA). All data were presented as means ± standard deviations.

Results and Discussion

FTIR

CS is not only biocompatible and biodegradable, but it can also be cross-linked ionically by anions to form gels. On the other hand, nickel oxide NPs are attached to the rGO surfaces via electrostatic and covalent interactions. As nickel oxide is a superparamagnetic material, it can potentially facilitate targeted drug delivery in cancer treatment in the presence of a magnetic field. Structures of GO, CS, NiO, rGO/NiO and CS/rGO/NiO NCs are studied by using FT-IR (Figure 1). The spectrum of GO has peaks at 3412, 1631 and 1090 cm^{-1}. These peaks are assigned to vibrations of –OH, C=O and C=C groups, respectively. The spectrum of NiO NPs displays peaks at 459 and 534 cm^{-1}. Both peaks are attributed to Ni-O stretching vibrations. In the spectrum of rGO/NiO, the height of the GO peaks is much lower than that in the spectrum of

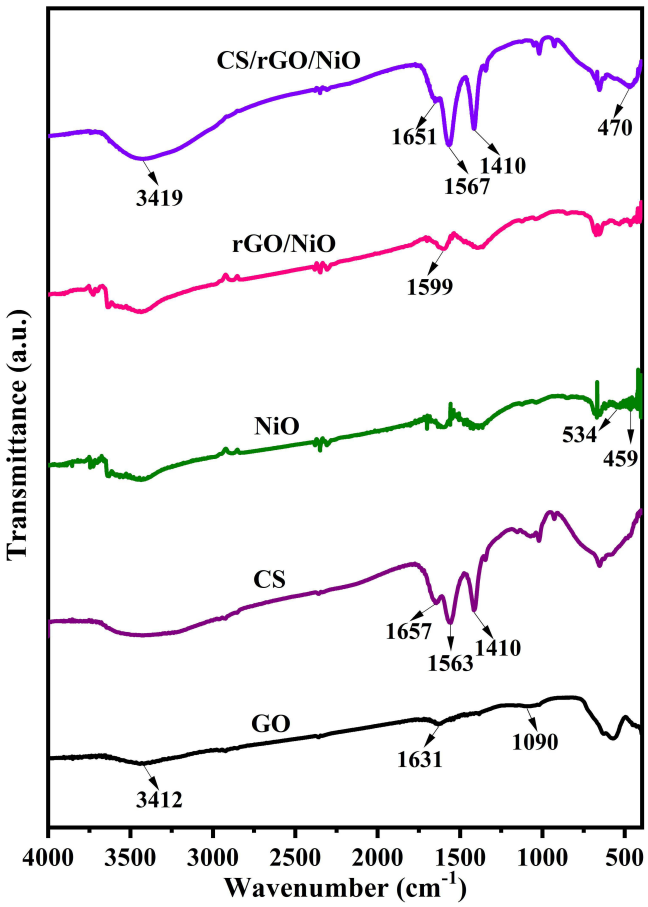

Figure 1 FTIR spectra of GO, CS, NiO, rGO/NiO and CS/rGO/NiO.

GO. Furthermore, the peak at 1631 cm^{-1} in the spectrum of GO shifts to 1599 cm^{-1} in the spectrum of rGO/NiO. This reveals the reduction of GO to rGO. In the spectrum of CS, three prominent peaks are observed at 1657 1559 and 1410 $cm^{-1.}$ These peaks are attributed to C=O stretching vibrations (amide I), N–H bending vibrations (amide II) and –C–O stretching vibrations of the primary alcoholic group, respectively. These peaks undergo a small shift in the spectrum of CS/rGO/NiO NC. This indicates the successful coating of CS on the surface of NiO NPs and rGO. In addition, in the spectrum of CS/rGO/NiO NC, a broad peak at 470 cm^{-1} is found, indicating the presence of NiO NPs. The peak at 3436 cm^{-1} (–OH) in the spectrum of CS shifts to a higher wavenumber in the spectrum of CS/rGO/NiO NCs. This can be explained by an increase in the extent of hydrogen-bonding interactions between CS and NiO/rGO.[20]

XRD

The XRD patterns of GO, CS, NiO NPs, rGO/NiO (1, 3, 5%) NCs and CS/rGO/NiO (5, 10, 15%) are presented in Figure 2. The peaks corresponding to GO are found at 10.50° to 23.4°. The broadening and shift of these peaks in the XRD pattern of rGO/NiO NCs (1%) is explained by reduction of GO and by interactions between rGO and NiO. The XRD pattern of rGO/NiO containing a lower concentration of GO shows peaks at 37.42, 43.3, 63.02 and 75.6°, which are attributed to (111), (200), (220) and (311) planes, respectively.

In addition, the XRD pattern of GO shows a peak at 10.5°, indicating the generation of GO from graphite. The peaks attributed to the metallic nickel phase can be found at 37.52, 43. 45, 63.24 and 75.8°. These peaks are assigned to (111), (200), (220) and (311) planes of nickel in the face-centered cubic structure, respectively.[21,22] In the XRD pattern of CS, two broad peaks are observed at 10.0° and 20.0°. The broad peak at 25.0° is attributed to the addition of CS to rGO/NiO. In the XRD pattern of CS/rGO/NiO, the peaks of CS disappear because strong interactions between rGO/NiO and CS make the amorphous nature of CS

https://doi.org/10.2147/IJN.S489418

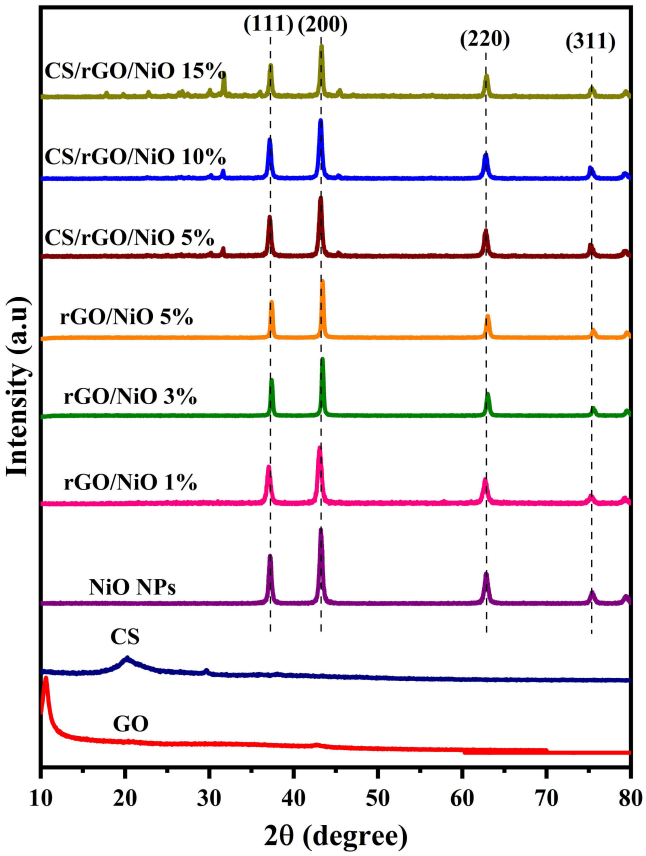

Figure 2 XRD patterns for synthesized GO, CS, NiO, rGO/NiO (1, 3, 5%) and CS/rGO/NiO (5, 10, 15%).

dominant. Upon an increase in the concentration of CS, the height of the peaks at around 24–26° is reduced. This indicates the formation of CS/rGO/NiO NCs.[23] It is observed that reactions at different percentages of GO and CS do not affect the crystalline structure of NiO NPs, with no apparent difference among different rGO concentrations (1, 3, and 5%) and CS concentrations (5, 10, and 15%) being found.

FE-SEM and HR-TEM

The morphological features of GO, CS, NiO NPs, and CS/rGO/NiO are shown in Figure 3. The SEM image of GO reveals that the nanosheets are interconnected to each other to form a network having a high surface area. In the case of CS, the small particles are agglomerated to form clusters with irregular shape. On the other hand, NiO NPs exhibit a particle size distribution of 30–35 nm and are almost free from agglomeration. The latter is an essential feature for the superparamagnetic property. In the case of CS/rGO/NiO NCs, the particles on the surface of GO are found to be aggregated to a large size due to (i) the agglomeration of NiO NPs and (ii) interactions with CS. The presence of compositions in rGO/NiO NCs and CS/rGO/NiO NCs is verified by the corresponding EDX spectra.

Apart from FE-SEM, CS/rGO/NiO is examined by using HR-TEM (Figure 4). The HR-TEM images of CS/rGO/NiO NCs show a uniform distribution of NiO and CS with a deformed spherical shape, mostly on the surface of a uniformly arranged rGO layer. The NiO and CS particles on the rGO surface in CS/rGO/NiO are clearly recognized. The crystal structure of NiO NPs embedded in the CS/rGO/NiO NCs is analyzed by selected area electron diffraction (SAED), with the SAED patterns obtained being shown in Figure 4D. The diffraction dots and rings represent the corresponding crystalline planes in NiO. This correlates well with the XRD data. The aggregation of NiO NPs is a clear indication for the electrostatic interactions between the carboxyl groups of GO and the amido groups of CS mediated by glutaraldehyde.

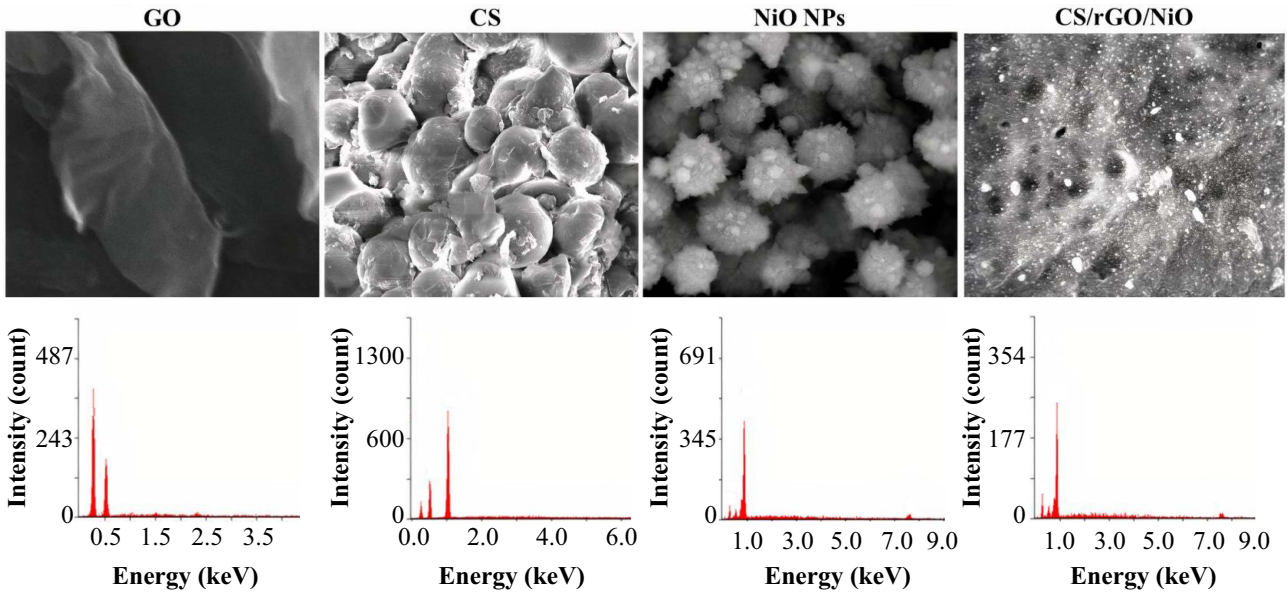

Figure 3 FE-SEM images of GO, CS, NiO, and CS/rGO/NiO and the corresponding EDX patterns.

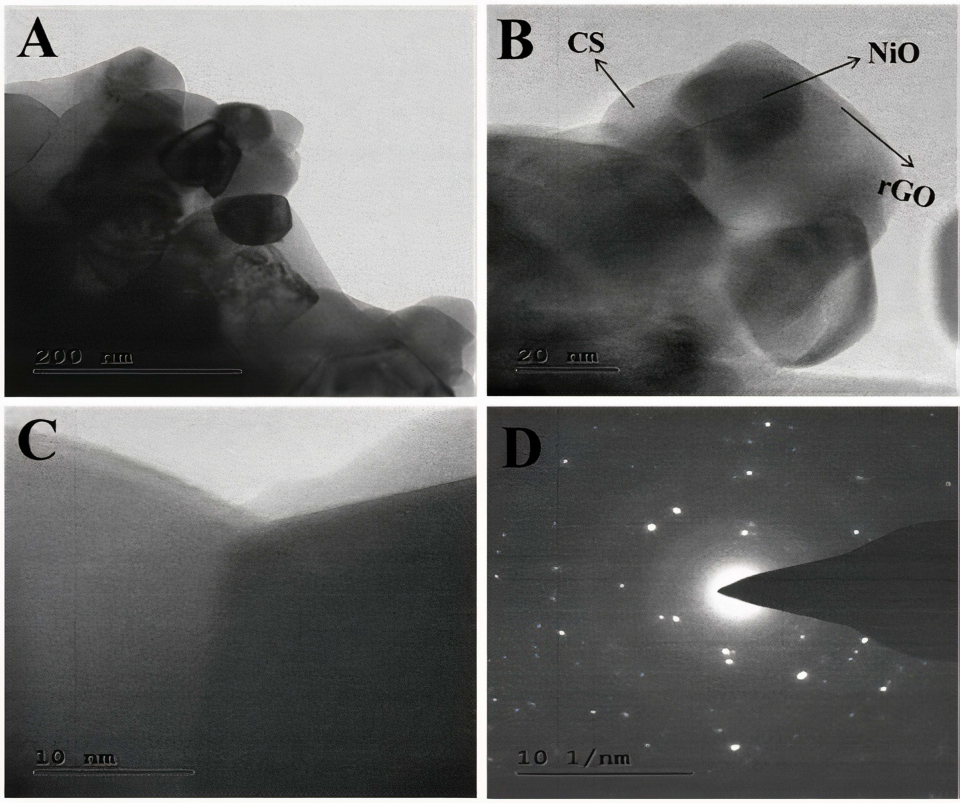

Figure 4 (**A**–**C**) HR-TEM images, with different magnifications, of CS/rGO/NiO. (**D**) The SAED pattern of CS/rGO/NiO.

XPS

XPS analysis on CS/rGO/NiO confirms the presence of the oxidized surface (Figure 5). The C 1s spectrum displays the asymmetric-line feature of graphite. The binding energy (BE) of the strongest Ni $2p_{3/2}$ element is greater than 855 eV.

https://doi.org/10.2147/IJN.S489418

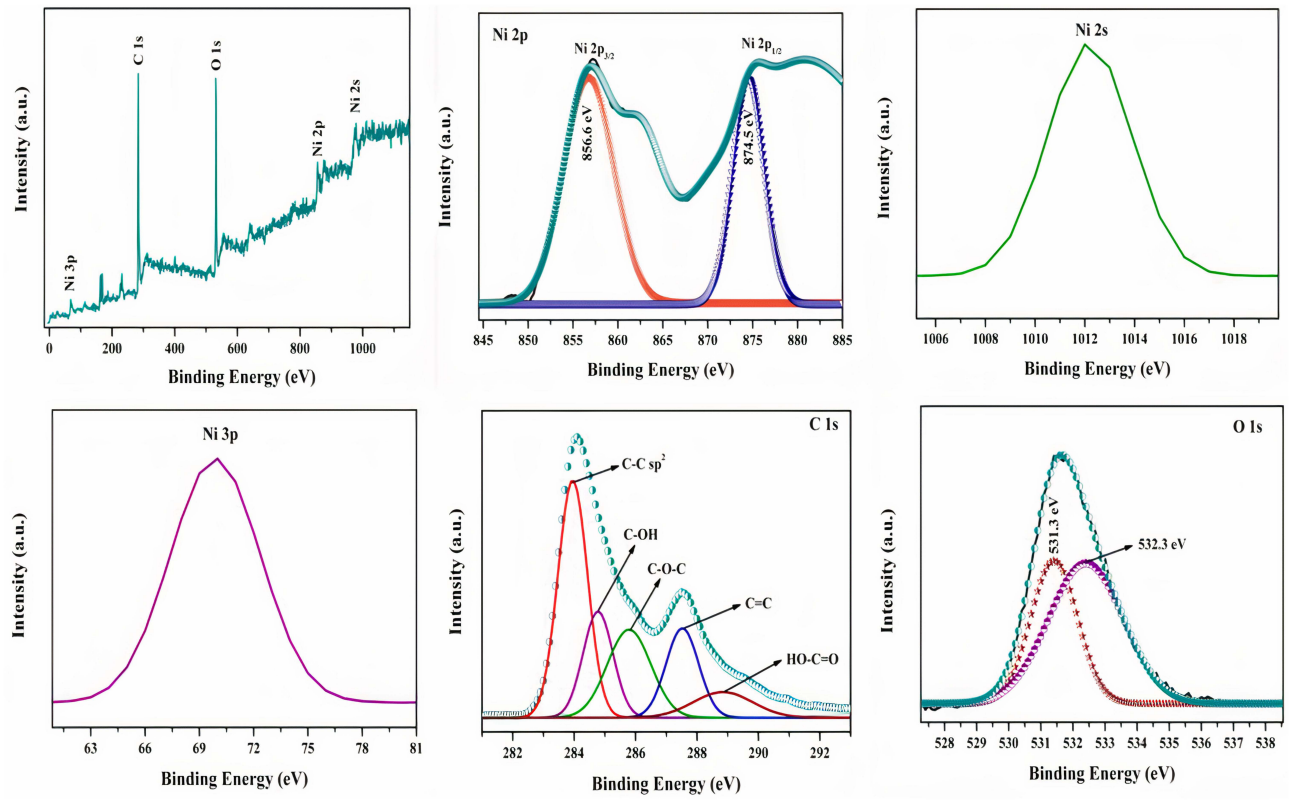

Figure 5 XPS spectrum of CS/rGO/NiO and the high-resolution spectra of Ni 2p, Ni 2s, Ni 3p, C 1s and O 1s peaks.

A thorough review of the NIST XPS database reveals that the majority of NiO BE values is less than 855 eV. This is attributed to the oxidized surface layer of the sample ($Ni(OH)_2$). In addition, the small shoulders detected at BE 853 eV indicate the existence of metallic nickel. Peaks at 284.5, 285.6, 287.5, and 289.0 eV in the C 1s spectrum are attributed to C-C/C=C, C-O, C-O-C/C=O, and O-C=O groups, respectively.[24,25] When the concentration of GO is reduced, the height of the C-O and C-O-C/C=O peaks decreases dramatically, but the height of the sp^2 carbon peak increases. This reveals the removal of oxygen-containing groups. The O 1s XPS spectrum shows three peaks at 529.3, 531.0 and 530.2 eV, These peaks are attributed to the lattice O in NiO, to HO–C=O groups on rGO, and to Ni–O–C, respectively. Strong interactions among rGO, NiO and CS in CS/rGO/NiO are revealed by the shift of the O 1s spectrum towards a higher BE. The formation of the Ni–O–C bond facilitates electron transfer among rGO, NiO and CS. For materials with a nanostructure, assignment of the surface layer composition is technically challenging. Yet, based on the available data, the presence of an oxidized surface layer (having a thickness of 5 nm at least in some areas covering the metallic Ni particles) is noted.

Determination of Magnetic Properties

The room temperature M-H loop of CS/rGO/NiO is shown in Figure 6. The NCs are found to be superparamagnetic, with the value of saturation magnetization (MS) being 35.3 emu/g. This is attributed to the presence of NiO NPs. Here, it is worth noting that the M_S value is lower compared to that of pure NiO NPs.[26] This may be due to the presence of a large quantity of materials (eg, rGO and CS) which do not possess magnetic properties. Nevertheless, the NCs respond to an external magnetic field. Remnant magnetization (M_R) and coercive field (H_C) are found to be 9.2 emu/g and 0.37 kOe, respectively. This confirms that NiO NPs influence the superparamagnetic property of CS/rGO/NiO. Our result suggests that the NCs can potentially serve as a T_2 material for magnetic resonance imaging (MRI) in the future.

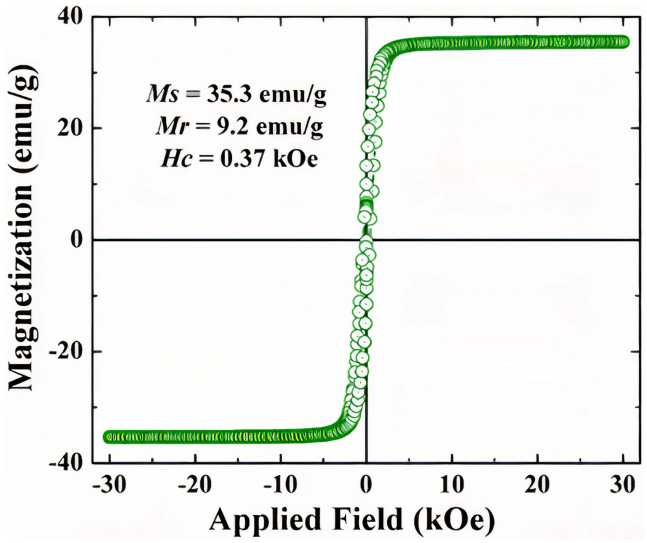

Figure 6 The room temperature M-H loop of CS/rGO/NiO.

Antimicrobial Activity

The antibacterial capability of the generated NCs is expected to come from NiO NPs, which possess antibacterial activity as previously reported.[27] In this study, we observe that NiO NPs outperform other samples in antibacterial activity as shown by the size of the resulting zone of inhibition (Figure 7A). Such activity is the result of (i) the production of reactive oxygen species (ROS) upon visible light illumination and (ii) of the generation of HO during lipid peroxidation.[28] The result of our antifungal test also indicates that all samples lead to stress experienced by fungal hyphae (Figure 7B). We propose that the NiO NPs and the NP-containing samples induce irreversible damage to the microbial strains, resulting in physical disruption to the plasma membrane and the release of intracellular material.[29] Furthermore, owing to the ability of *S. pneumoniae, P. aeruginosa*, and *C. albicans* to form biofilms, these microbial

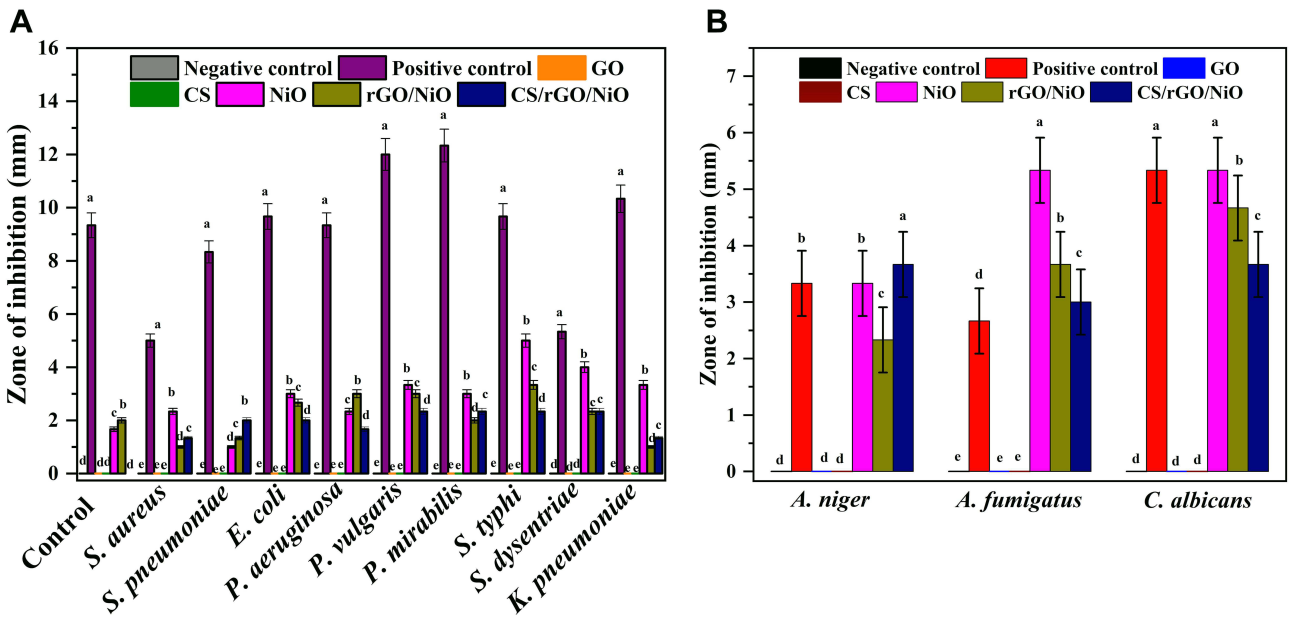

Figure 7 Antimicrobial activity of GO, CS, NiO, rGO/NiO and CS/rGO/NiO against (A) bacteria and (B) fungi. Treatment with DMSO alone was used for the negative control. Treatment with azithromycin (for bacteria) and fluconazole (for fungi) was used for the positive control. Within each species, different letters above each bar indicate significant differences among treatments (ANOVA, Tukey's HSD test, $p < 0.05$).

https://doi.org/10.2147/IJN.S489418

strains are used to study the inhibitory effects of GO, CS, NiO, rGO/NiO, and CS/rGO/NiO on biofilm formation under confocal laser scanning microscopy (CLSM) (Figure 8). More than 90% of biofilm inhibition is seen after treatment with NiO. Eighty-five percent of biofilm inhibition is observed after treatment with rGO/NiO. Seventy-five percent of biofilm inhibition is observed after treatment with CS/rGO/NiO. The generation of ROS may partially contribute to inhibition of biofilm formation.

Performance in Drug Delivery

To determine the performance of the CS/rGO/NiO/FA NCs in drug delivery, DOX is used as a model drug. To confirm the successful loading of DOX into NCs, analysis by UV-vis spectroscopy is performed (Figure 9). Pure DOX shows an absorption wavelength at 481 nm, whereas the absorption peak of DOX-loaded NCs exhibits a red shift. This implies that hydrogen bonding develops between DOX and the NCs, confirming that DOX is successfully encapsulated. The absorbance of the NCs at 481 nm increases when the amount of DOX loaded into the NCs increases. The concentration of DOX loaded into the NCs is saturated at 0.498 mg/mL^{-1} (Figure 10A). This is higher than the efficiency of other NCs reported in the literature.[12]

The process of drug loading is partially mediated by hydrogen bonding between DOX and rGO as well as between DOX and CS. This is consistent with the findings of Hazhir and coworkers,[30] who reported that the formation of hydrogen bonds between DOX and CS/rGO plays a role in mediating drug loading. The process of drug loading into our NCs may also be facilitated by π–π stacking and hydrophobic interactions between DOX and rGO. The possibility of this is partially supported by the work of Vovusha and coworkers,[31] who found that DOX interacts with GO via π–π stacking and hydrogen bonding interactions. The drug release behavior of our NCs is studied in a simulated physiological environment using a Na_2HPO_4-KH_2PO_4 buffer solution (pH 7.4 and 5.5) at 37°C. The rate of drug release is more rapid in acidic conditions (pH 5.5) than in neutral conditions (pH 7.4) (Figure 10B). This pH-responsive-release behavior may reduce the systemic toxicity of DOX in the future when the NCs are used as a drug carrier, thereby potentially minimizing toxicity on normal cells during chemotherapy or other treatment regimes.[32–34]

To understand the release kinetics, the release data are fitted into different kinetic models (including the zero-order model, first-order model, and the Higuchi model). Furthermore, to investigate the drug release mechanism, 60% of the release data are fitted into the Korsmeyer-Peppas equation (Table 1). The release kinetics fits the first-order model the

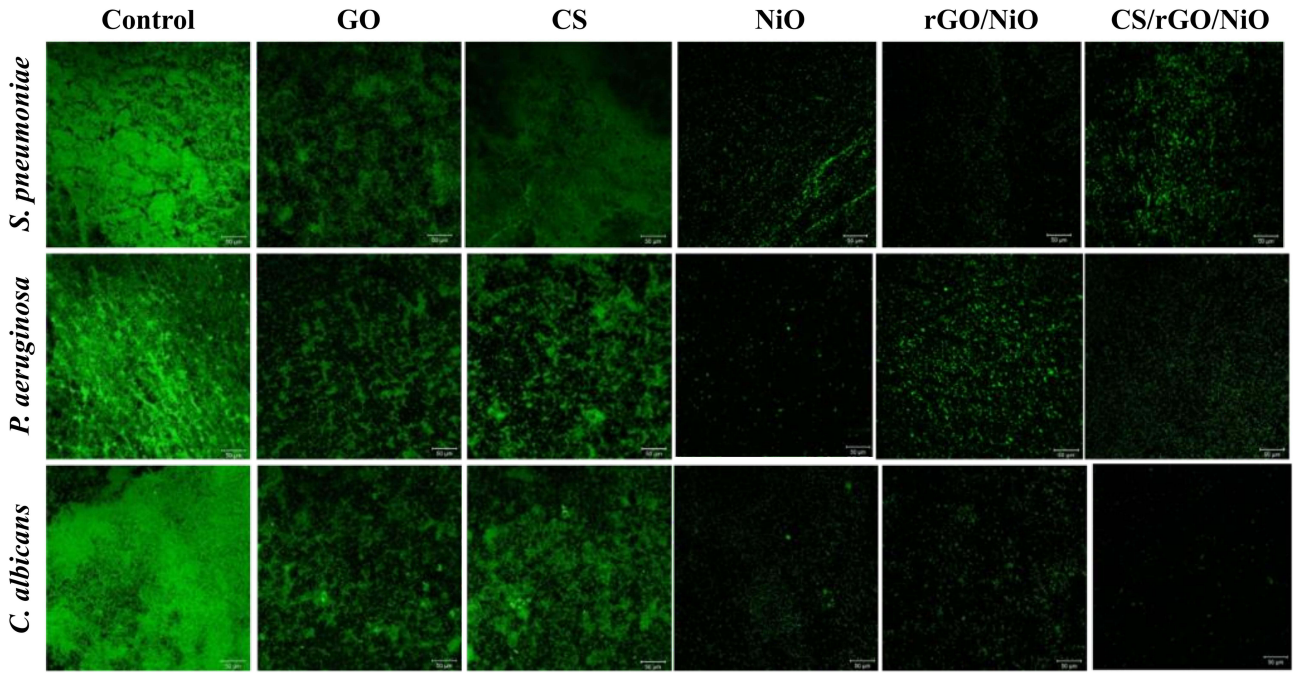

Figure 8 CLSM images of biofilms exposed to different samples at 37 °C for 24 h. In the images, live microbes emit green light. Dead cells are not colored. Treatment with DMSO alone was used as the control.

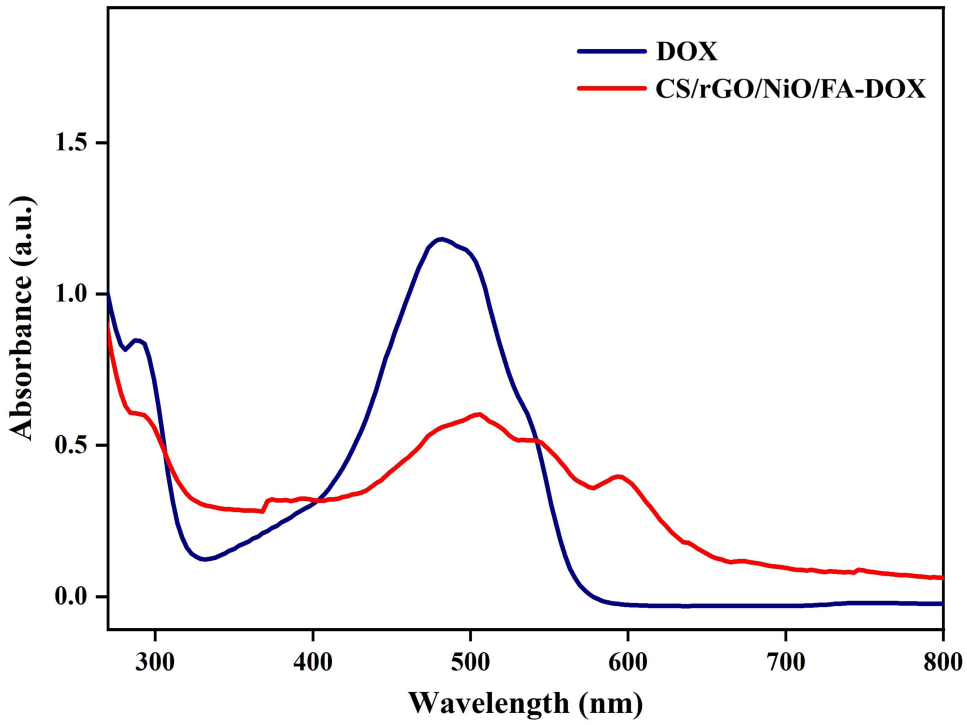

Figure 9 UV-vis absorption spectra of DOX and DOX-loaded CS/rGO/NiO/FA NCs.

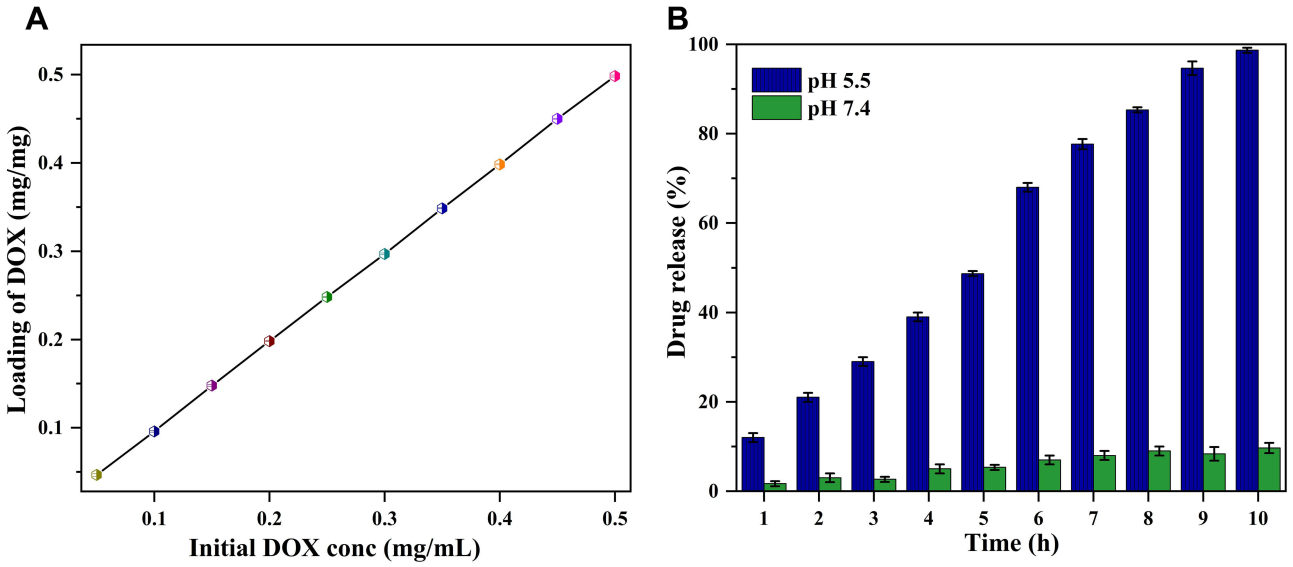

Figure 10 (**A**) Changes in the efficiency of DOX loading into CS/rGO/NiO/FA NCs at different initial DOX concentrations. (**B**) The percentage of drug release from DOX-loaded CS/rGO/NiO/FA NCs at different pH values.

most, suggesting that the DOX-loaded CS/rGO/NiO/FA NCs release DOX molecules with respect to time.[35] Results of analysis using the Korsmeyer-Peppas equation reveal that the value of the release exponent *n* is between 0.887 and 1.102, indicating that release of DOX from DOX-loaded CS/rGO/NiO/FA NCs follows the super case II transport mechanism, with the release rate governed by the relaxation and degradation of the polymer matrix.

https://doi.org/10.2147/IJN.S489418

Table 1 Release Kinetics Parameters of DOX-Loaded CS/rGO/NiO/FA NCs at Different pH Values

pH	Zero-Order		First-Order		Higuchi		Korsmeyer-Peppas	
	K_0	r^2	K_1	r^2	K_H	r^2	n	r^2
5.5	10.424	0.987	0.180	0.878	27.058	0.813	1.102	0.977
7.4	1.049	0.928	0.011	0.937	2.760	0.859	0.887	0.922

Toxicity and Biocompatibility

The toxicity of CS/rGO/NiO, DOX-loaded CS/rGO/NiO, and DOX-loaded CS/rGO/NiO/FA in A549 and MCF7 cells is evaluated by using the MTT assay (Figure 11A and B). The viability of cells treated with DOX-loaded CS/rGO/NiO/FA is lower compared to that of those treated with CS/rGO/NiO and DOX-loaded CS/rGO/NiO. This is partially due to the interactions between DOX-loaded CS/rGO/NiO/FA and the folate receptors of the cells, thereby facilitating cellular uptake of the drug-loaded NCs.[36] To understand the induction of apoptosis, the cells are treated with the IC_{50} concentrations of CS/rGO/NiO, DOX-loaded CS/rGO/NiO, and DOX-loaded CS/rGO/NiO/FA. After that, they are stained with acridine orange (AO) and DAPI and are assessed under a fluorescence microscope (Figure 12A and B). AO infiltrates into the plasma membrane of the normal cells and gives green fluorescence, whereas the apoptotic cells appear as orange-colored entities due to nuclear shrinking and membrane blabbing. Necrotic cells give red fluorescence due to the destruction of the membrane integrity.[37] Cell death induced by the DOX-loaded CS/rGO/NiO and DOX-loaded CS/rGO/NiO/FA may be mediated by DNA damage and oxidative stress. DAPI labeling is used in this study to differentiate apoptotic nuclei from healthy ones.[38–40] Healthy cells are found to have an intact spherical nucleus and give weak fluorescence. Yet, after treatment with DOX-loaded CS/rGO/NiO and DOX-loaded CS/rGO/NiO/FA, nucleus fragmentation is observed, with compressed nuclei found. This corroborates the effect of DOX-loaded CS/rGO/NiO and DOX-loaded CS/rGO/NiO/FA in inducing apoptosis.[41,42]

The biocompatibility of the NCs is evaluated in vivo by using zebrafish embryos as a model. Because zebrafish and human are so similar in their genomes, data collected from zebrafish embryos can provide information on the toxicity of our NPs on vertebrates. The development of the embryo is monitored microscopically at 0 hpf and 72 hpf to assess the hatching percentage after treatment with GO, CS, NiO, rGO/NiO, and CS/rGO/NiO (Figure 13). The hatching percentages are 81.6%, 88.3%, 93%, 91%, and 94.6% after treatment with NiO NPs, GO, CS, rGO/NiO, and CS/rGO/NiO,

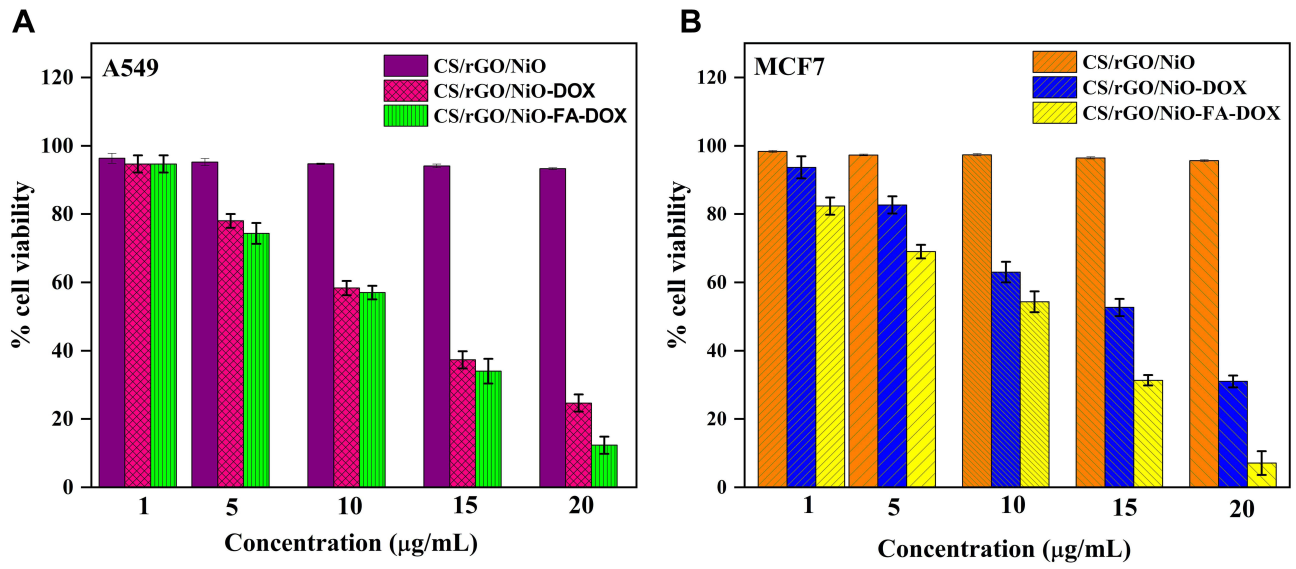

Figure 11 The viability of (**A**) A549 and (**B**) MCF7 cells upon treatment with different concentrations of CS/rGO/NiO, DOX-loaded CS/rGO/NiO and DOX-loaded CS/rGO/NiO/FA.

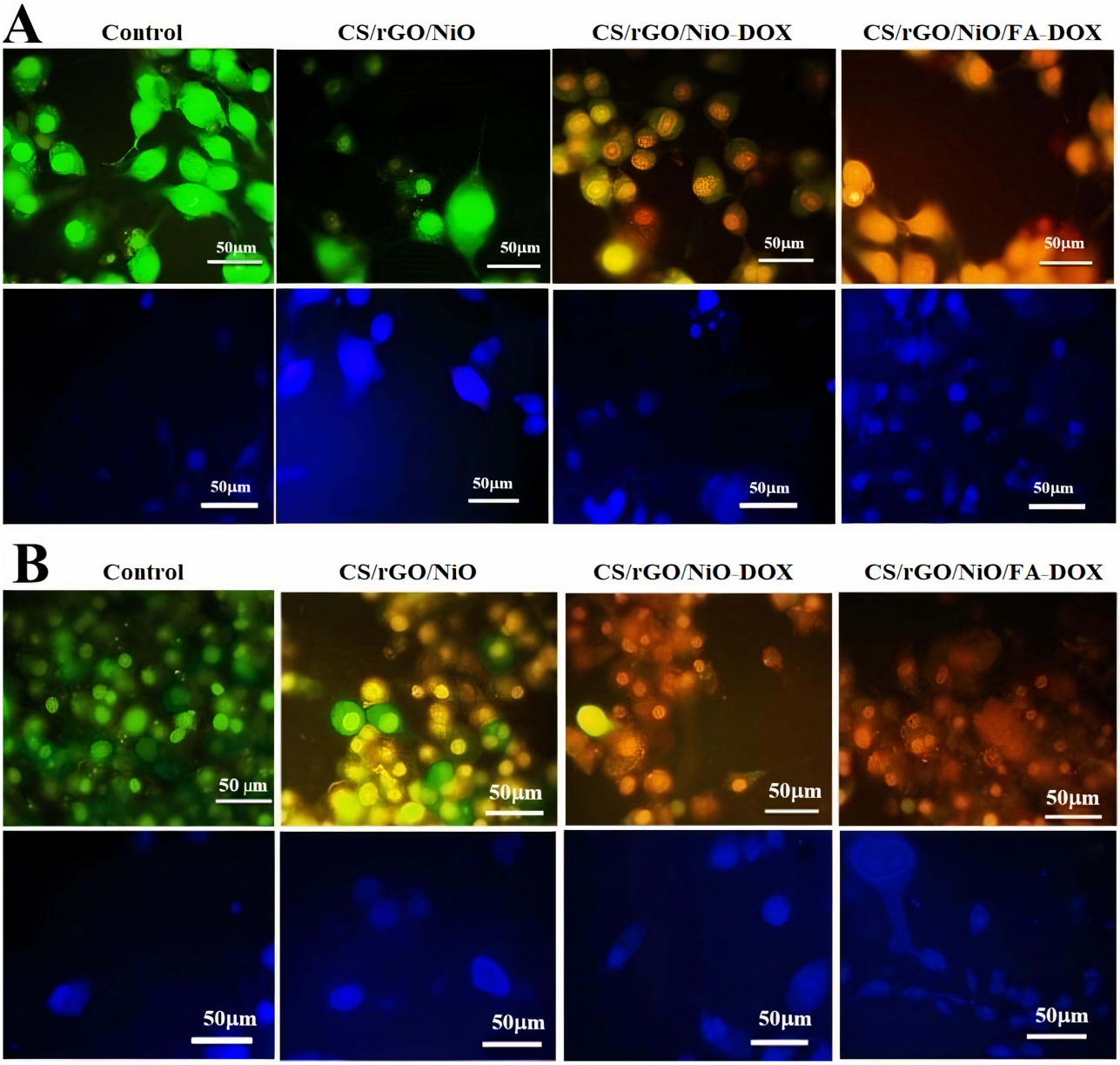

Figure 12 Fluorescence images of stained (**A**) A549 and (**B**) MCF7 cells after treatment with CS/rGO/NiO, DOX-loaded CS/rGO/NiO, and DOX-loaded CS/rGO/NiO/FA. Untreated cells are used as the control.

respectively. In a previous study, Kovrižnych and coworkers reported that treatment with NiO NPs at a concentration of 6.25mg/mL for 30 days leads to no apparent mortality in *Danio rerio*.[43] In the present study, the hatching rate is still over 80% after treatment with NiO NPs for 72 hours. This indicates the low toxicity of NiO NPs. Despite this, zebrafish embryos injected with NiO NPs show defects such as unclear anatomy, neonatal mortality, and impaired movement. These defects are observed in 20% of the treated embryos. On the other hand, no abnormalities are identified in those injected with GO, CS, rGO/NiO, and CS/rGO/NiO (Figure 14). This suggests that the biocompatibility of NiO NPs is significantly enhanced upon incorporation into the NCs.

Conclusion

This study reports folate-conjugated CS/rGO/NiO NCs as a multifunctional carrier for drug delivery. The NCs, upon being loaded with DOX, exhibit pH-responsive drug release behavior. In A549 and MCF7 cells, both DOX-loaded CS/rGO/NiO and

https://doi.org/10.2147/IJN.S489418

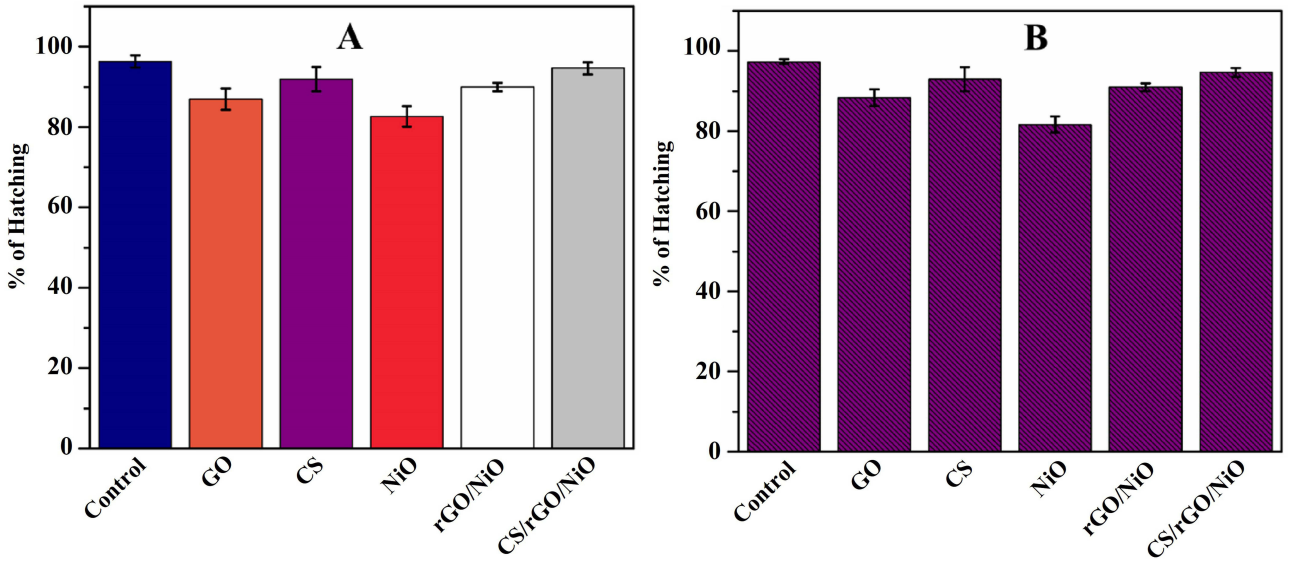

Figure 13 The hatching rates of zebrafish embryos, observed at (**A**) 0 and (**B**) 72 hpf, after treatment with GO, CS, NiO, rGO/NiO and CS/rGO/NiO. The control group receives no treatment.

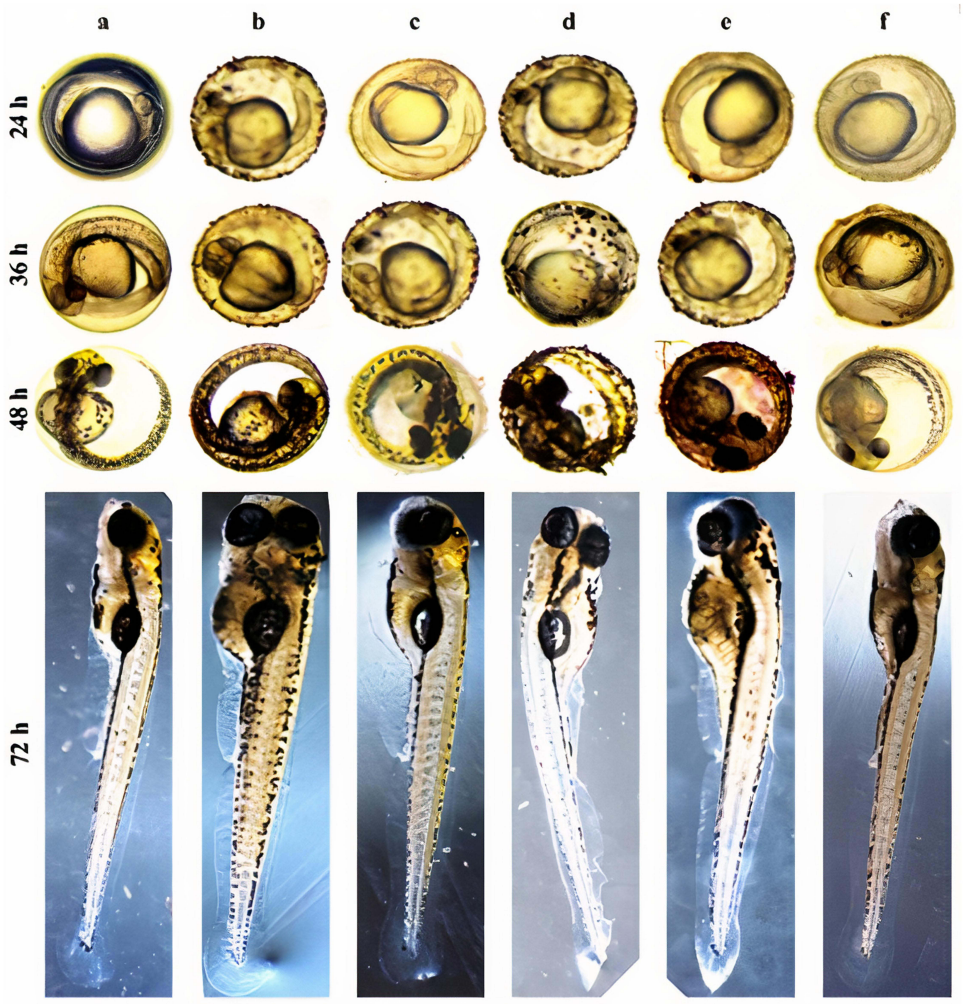

Figure 14 Microscopic images of the zebrafish taken, after different time intervals (24 h, 36 h, 48 h and 72 h), upon microinjection of different samples into zebrafish embryos: (**a**) control, (**b**) GO, (**c**) CS, (**d**) NiO, (**e**) rGO/NiO and (**f**) CS/rGO/NiO. The control group receives no treatment.

DOX-loaded CS/rGO/NiO/FA NCs are successfully taken up by the cells; however, DOX-loaded CS/rGO/NiO/FA NCs show higher efficiency in cellular internalization due to interactions between FA and the folate receptors. While DOX-loaded NCs lead to a drastic drop in the viability of A549 and MCF7 cells, by using zebrafish as a model, the excellent biocompatibility of the NCs is confirmed. To further explore their real-world applicability and facilitate clinical translation, in vivo and clinical evaluations will be necessary. Despite this, the carrier functions as a controlled-release system for bioactive agents, highlighting its potential for biomedical applications. Along with their intrinsic antibacterial and antifungal activity, our reported NCs show high potential for future applications as a drug carrier in diverse treatment regimes, ranging from chemotherapy to anti-infective therapy. This study has demonstrated the developed DOX-loaded NCs showed potential anticancer activity on MCF-7 and A549 cells; to further investigate the potential of the carrier for real-world application and to facilitate clinical translation, in vivo and clinical evaluation will be required in the future. Despite this, the developed carrier acts as a controlled-release carrier for the release of bioactive agents; hence, the developed carrier has potential for biomedical applications.

Data Sharing Statement

All data generated or analysed are included in this published article.

Acknowledgments

This research was funded by the DST-PURSE [SR/PURSE Phase 2/38 (G)], Department of Education, Government of India.

Author Contributions

All authors made a significant contribution to the conception, study design, execution, data acquisition, and data analysis. They took part in drafting, revising or critically reviewing the article. They gave final approval of the version to be published and agreed on the journal to which the article was submitted. They agreed to be accountable for all aspects of the work.

Disclosure

The authors report no conflicts of interest in this work.

References

1. Lv Y-C, Esmaeili Shahri E, Mahmoudi A, Keifi Naughabi R, Abbaspour S, Tayebee R. Bioinspired nickel oxide nanoparticle as an efficient nanocarrier in the delivery of doxorubicin as an anti-bladder cancer drug. *Inorg Chem Commun*. 2023;152:110650. doi:10.1016/j.inoche.2023.110650
2. Punitha U, Mary Saral A. Nickel oxide nanoparticles from Sargassumwightii: synthesis, Characterization, and biomedical applications. *Results Chem*. 2024;7:101289. doi:10.1016/j.rechem.2023.101289
3. AlSalhi MS, Aziz MH, Atif M, et al. Synthesis of NiO nanoparticles and their evaluation for photodynamic therapy against HeLa cancer cells. *J King Saud Univ Sci*. 2020;32(2):1395–1402. doi:10.1016/j.jksus.2019.11.033
4. Aarthi J, Kaviya SS, Kirubavathi K, et al. Green synthesis of nickel oxide nanoparticles using leaf extract of Mimosa pudica for killing triple-negative breast cancer MDA-MB-231 cells and bacteria. *J Mol Struct*. 2025;1321:140178. doi:10.1016/j.molstruc.2024.140178
5. Lu Y, Han M, Esmaeili Shahri E, Abbaspour S, Tayebee R. Delivery of anti-cancer and anti-depression doxepin drug by nickel oxide nanoparticles originated from the Cressa nudicaulis plant extract. *RSC Adv*. 2023;13(18):12133–12140. doi:10.1039/D2RA07545H
6. Kouhbanani MAJ, Sadeghipour Y, Sarani M, et al. The inhibitory role of synthesized Nickel oxide nanoparticles against Hep-G2, MCF-7, and HT-29 cell lines: the inhibitory role of NiO NPs against Hep-G2, MCF-7, and HT-29 cell lines. *Green Chem Lett Rev*. 2021;14(3):444–454. doi:10.1080/17518253.2021.1939435
7. Mohammedsaleh ZM, Saleh FM. Reduced graphene oxide for selective administration of rutin toward the cancer cell therapy. *J Drug Delivery Sci Technol*. 2023;83:104397. doi:10.1016/j.jddst.2023.104397
8. Obireddy SR, Lai W-F. Multi-component hydrogel beads incorporated with reduced graphene oxide for ph-responsive and controlled co-delivery of multiple agents. *Pharmaceutics*. 2021;13(3):313. doi:10.3390/pharmaceutics13030313
9. Dhanavel S, Revathy TA, Sivaranjani T, et al. 5-Fluorouracil and curcumin co-encapsulated chitosan/reduced graphene oxide nanocomposites against human colon cancer cell lines. *Polym Bull*. 2020;77(1):213–233. doi:10.1007/s00289-019-02734-x
10. Mary Deena D, Prabhu S, Vilwanathan R, Philominal A. Anticancer activity of manganese dioxide/reduced graphene oxide nanocomposites against A549 human lung adenocarcinoma cell line. *Nano-Struct Nano-Objects*. 2023;35:101032. doi:10.1016/j.nanoso.2023.101032
11. Kazemi S, Pourmadadi M, Yazdian F, Ghadami A. The synthesis and characterization of targeted delivery curcumin using chitosan-magnetite-reduced graphene oxide as nano-carrier. *Int J Biol Macromol*. 2021;186:554–562. doi:10.1016/j.ijbiomac.2021.06.184
12. Karthika V, AlSalhi MS, Devanesan S, Gopinath K, Arumugam A, Govindarajan M. Chitosan overlaid Fe3O4/rGO nanocomposite for targeted drug delivery, imaging, and biomedical applications. *Sci Rep*. 2020;10(1):18912. doi:10.1038/s41598-020-76015-3

13. Lai WF, Lin MC. Folate-conjugated chitosan-poly(ethylenimine) copolymer as an efficient and safe vector for gene delivery in cancer cells. *Curr Gene Ther*. 2015;15(5):472–480. doi:10.2174/1566523215666150812120347
14. Yang S-J, Lin F-H, Tsai K-C, et al. Folic acid-conjugated chitosan nanoparticles enhanced protoporphyrin ix accumulation in colorectal cancer cells. *Bioconjugate Chem*. 2010;21(4):679–689. doi:10.1021/bc9004798
15. Chen Q, Zheng J, Yuan X, Wang J, Zhang L. Folic acid grafted and tertiary amino based pH-responsive pentablock polymeric micelles for targeting anticancer drug delivery. *Mater Sci Eng C*. 2018;82:1–9. doi:10.1016/j.msec.2017.08.026
16. Norizan MN, Moklis MH, Ngah Demon SZ, et al. Carbon nanotubes: functionalisation and their application in chemical sensors. *RSC Adv*. 2020;10 (71):43704–43732. doi:10.1039/D0RA09438B
17. Panda PK, Dash P, Yang J-M, Chang Y-H. Development of chitosan, graphene oxide, and cerium oxide composite blended films: structural, physical, and functional properties. *Cellulose*. 2022;29(4):2399–2411. doi:10.1007/s10570-021-04348-x
18. Zhang W, Dang G, Dong J, et al. A multifunctional nanoplatform based on graphitic carbon nitride quantum dots for imaging-guided and tumor-targeted chemo-photodynamic combination therapy. *Colloids Surf B Biointerfaces*. 2021;199:111549. doi:10.1016/j.colsurfb.2020.111549
19. Rathnam SR, Reddy OS, Aravind S, Lai W-F, Patwari SB. Development of pH-sensitive microbeads incorporated with amine-functionalized magnetic nanoparticles for enhanced antibacterial activity. *ChemistrySelect*. 2024;9(37):e202400340. doi:10.1002/slct.202400340
20. Zhu Y, Chu W, Wang N, et al. Self-assembled Ni/NiO/RGO heterostructures for high-performance supercapacitors. *RSC Adv*. 2015;5 (95):77958–77964. doi:10.1039/C5RA14790E
21. Pilban Jahromi S, Pandikumar A, Goh BT, et al. Influence of particle size on performance of a nickel oxide nanoparticle-based supercapacitor. *RSC Adv*. 2015;5(18):14010–14019. doi:10.1039/C4RA16776G
22. Zhang J, Zeng D, Zhao S, et al. Room temperature NO2 sensing: what advantage does the rGO–NiO nanocomposite have over pristine NiO? *Phys Chem Chem Phys*. 2015;17(22):14903–14911. doi:10.1039/C5CP01987G
23. Ashiri S, Mehdipour E. Preparation of a novel palladium catalytic hydrogel based on graphene oxide/chitosan NPs and cellulose nanowhiskers. *RSC Adv*. 2018;8(57):32877–32885. doi:10.1039/C8RA06623J
24. Han D, Yan L, Chen W, Li W. Preparation of chitosan/graphene oxide composite film with enhanced mechanical strength in the wet state. *Carbohydr Polym*. 2011;83(2):653–658. doi:10.1016/j.carbpol.2010.08.038
25. Lu A, Chen Y, Li H, et al. Magnetic metal phosphide nanorods as effective hydrogen-evolution electrocatalysts. *Int J Hydrogen Energy*. 2014;39 (33):18919–18928. doi:10.1016/j.ijhydene.2014.09.104
26. Ramesan MT, Nidhisha V, Jayakrishnan P. Facile synthesis, characterization and material properties of a novel poly(vinyl cinnamate)/ nickel oxide nanocomposite. *Polym Int*. 2017;66(4):548–556. doi:10.1002/pi.5288
27. Nazanin H, Nima Hosseini J, Saber Y. Evaluation of the Antibacterial Effects of Nickel Nanoparticles on Biofilm Production by Streptococcus mutans. *J Med Bacteriol*. 2017;6(1–2):8–14.
28. Angel Ezhilarasi A, Judith Vijaya J, Kaviyarasu K, John Kennedy L, Ramalingam RJ, Al-Lohedan HA. Green synthesis of NiO nanoparticles using Aegle marmelos leaf extract for the evaluation of in-vitro cytotoxicity, antibacterial and photocatalytic properties. *J Photochem Photobiol B: Biol*. 2018;180:39–50. doi:10.1016/j.jphotobiol.2018.01.023
29. Din MI, Nabi AG, Rani A, Aihetasham A, Mukhtar M. Single step green synthesis of stable nickel and nickel oxide nanoparticles from Calotropis gigantea: catalytic and antimicrobial potentials. *Environ NanotechnolMonitManag*. 2018;9:29–36.
30. Hazhir N, Chekin F, Raoof JB, Fathi S. A porous reduced graphene oxide/chitosan-based nanocarrier as a delivery system of doxorubicin. *RSC Adv*. 2019;9(53):30729–30735. doi:10.1039/C9RA04977K
31. Vovusha H, Banerjee D, Yadav MK, et al. Binding characteristics of anticancer drug doxorubicin with two-dimensional graphene and graphene oxide: insights from density functional theory calculations and fluorescence spectroscopy. *J Phys Chem C*. 2018;122(36):21031–21038. doi:10.1021/acs.jpcc.8b04496
32. Xu H, Cheng L, Wang C, Ma X, Li Y, Liu Z. Polymer encapsulated upconversion nanoparticle/iron oxide nanocomposites for multimodal imaging and magnetic targeted drug delivery. *Biomaterials*. 2011;32(35):9364–9373. doi:10.1016/j.biomaterials.2011.08.053
33. Zhu L, Wang D, Wei X, et al. Multifunctional pH-sensitive superparamagnetic iron-oxide nanocomposites for targeted drug delivery and MR imaging. *J Control Release*. 2013;169(3):228–238. doi:10.1016/j.jconrel.2013.02.015
34. Xie M, Lei H, Zhang Y, et al. Non-covalent modification of graphene oxide nanocomposites with chitosan/dextran and its application in drug delivery. *RSC Adv*. 2016;6(11):9328–9337. doi:10.1039/C5RA23823D
35. Gagliardi M. Design and development of molecularly imprinted biodegradable polymers for nanomedicine. *Adv Ind Eng Polym Res*. 2023;6 (4):396–406.
36. Sathiyaseelan A, Saravanakumar K, Manivasagan P, Jeong MS, Jang E-S, Wang M-H. Folic acid conjugated chitosan encapsulated palladium nanoclusters for NIR triggered photothermal breast cancer treatment. *Carbohydr Polym*. 2022;280:119021. doi:10.1016/j.carbpol.2021.119021
37. Muthukumarasamyvel T, Rajendran G, Santhana Panneer D, Kasthuri J, Kathiravan K, Rajendiran N. Role of surface hydrophobicity of dicationic amphiphile-stabilized gold nanoparticles on A549 lung cancer cells. *ACS Omega*. 2017;2(7):3527–3538. doi:10.1021/acsomega.7b00353
38. Chang Y, Yang S-T, Liu J-H, et al. In vitro toxicity evaluation of graphene oxide on A549 cells. *Toxicol Lett*. 2011;200(3):201–210. doi:10.1016/j.toxlet.2010.11.016
39. Veiseh O, Gunn JW, Zhang M. Design and fabrication of magnetic nanoparticles for targeted drug delivery and imaging. *Adv Drug Deliv Rev*. 2010;62(3):284–304. doi:10.1016/j.addr.2009.11.002
40. Xie M, Zhang F, Liu L, et al. Surface modification of graphene oxide nanosheets by protamine sulfate/sodium alginate for anti-cancer drug delivery application. *Appl Surf Sci*. 2018;440:853–860. doi:10.1016/j.apsusc.2018.01.175
41. Huang S, Shao K, Liu Y, et al. Tumor-targeting and microenvironment-responsive smart nanoparticles for combination therapy of antiangiogenesis and apoptosis. *ACS Nano*. 2013;7(3):2860–2871. doi:10.1021/nn400548g
42. Karthika V, Kaleeswarran P, Gopinath K, et al. Biocompatible properties of nano-drug carriers using TiO2-Au embedded on multiwall carbon nanotubes for targeted drug delivery. *Mater Sci Eng C*. 2018;90:589–601. doi:10.1016/j.msec.2018.04.094
43. Kovrižnych JA, Sotníková R, Zeljenková D, Rollerová E, Szabová E. Long-term (30 days) toxicity of NiO nanoparticles for adult zebrafish Danio rerio. *Interdiscip Toxicol*. 2014;7(1):23–26. doi:10.2478/intox-2014-0004